ARTICLE

Chiral Transport of Hot Carriers in Graphene in the Quantum Hall Regime

Bin Cao,[△] Tobias Grass,[△] Olivier Gazzano, Kishan Ashokbhai Patel, Jiuning Hu, Markus Müller, Tobias Huber-Loyola, Luca Anzi, Kenji Watanabe, Takashi Taniguchi, David B. Newell, Michael Gullans, Roman Sordan, Mohammad Hafezi,* and Glenn S. Solomon*

Read Online

ACCESS | Metrics & More | Article Recommendations | SI Supporting Information

ABSTRACT: Photocurrent (PC) measurements can reveal the relaxation dynamics of photoexcited hot carriers beyond the linear response of conventional transport experiments, a regime important for carrier multiplication. Here, we study the relaxation of carriers in graphene in the quantum Hall regime by accurately measuring the PC signal and modeling the data using optical Bloch equations. Our results lead to a unified understanding of the relaxation processes in graphene over different magnetic field strength regimes, which is governed by the interplay of Coulomb interactions and interactions with acoustic and optical phonons. Our data provide clear indications of a sizable carrier multiplication. Moreover, the

oscillation pattern and the saturation behavior of PC are manifestations of not only the chiral transport properties of carriers in the quantum Hall regime but also the chirality change at the Dirac point, a characteristic feature of a relativistic quantum Hall effect.

KEYWORDS: *graphene, quantum Hall effect, photocurrent, carrier multiplication, carrier relaxation, Auger effect, chiral electron transport*
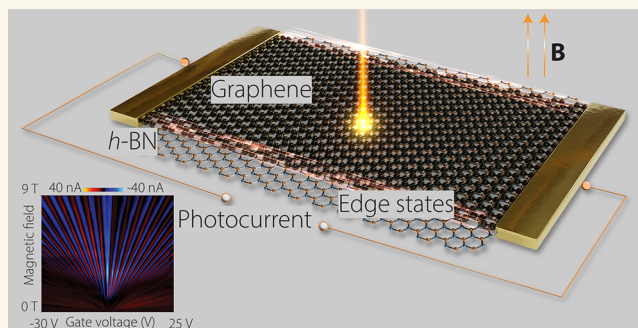
Chiral transport is a signature feature in many topological systems[1,2] and results from restrictions in the motion of a particle at the edge of a gapped two-dimensional system to a single direction.[1,3,4] In quantum Hall systems, the edge chirality of the charge carriers is determined by the direction of the magnetic field.[3,5,6] A special case is the quantum Hall effect in graphene where the relativistic nature of the electrons leads to particle-hole symmetry, and the absence of an intrinsic band gap allows for both the relaxation of carriers and the tunability of the Fermi level across the Dirac point. Importantly, carriers within Landau levels (LLs) across the Dirac point have opposite edge chirality,[7–10] with an exception of the zeroth LL (LL$_0$).[11–13] Therefore, in optical experiments which excite electrons from LLs far below the Dirac point to LLs high above, an interesting interplay occurs between carriers of different types (electrons and holes) within LLs of potentially different edge chiralities.[9,14] In particular, the edge chirality of a carrier may change during the relaxation process depending on the energy of the Fermi level with respect to the Dirac point, and in addition, the relaxation rates of electrons and holes may change and become unequal depending on the position of the Fermi level within a given LL. The result is a rich variety of photocurrent (PC) patterns, reflecting the interplay of topological properties of LLs as well

as the uncharacteristic relaxation dynamics, whose detailed measurements are reported here, along with a microscopic modeling and an intuitive picture that together form a cohesive explanation of the observed behavior, and at the same time provides insight in role of different relaxation channels, including carrier–carrier and carrier–phonon scattering.

Qualitative studies of the PC in the quantum Hall regime have been reported.[9,14–17] An intuitive picture based on a relaxation bottleneck for either excited electrons or excited holes has been given in ref 9, but invoking a competing interpretation, the PC has also been explained with heating effects.[15,16,18] A unified picture of the PC, based on and backed by a quantitative model, has still been missing. Possible contributions from carrier multiplication (CM)[9,19–21] have been considered in the context of hot carrier relaxation, but despite many attempts with optical methods,[22–24] definitive
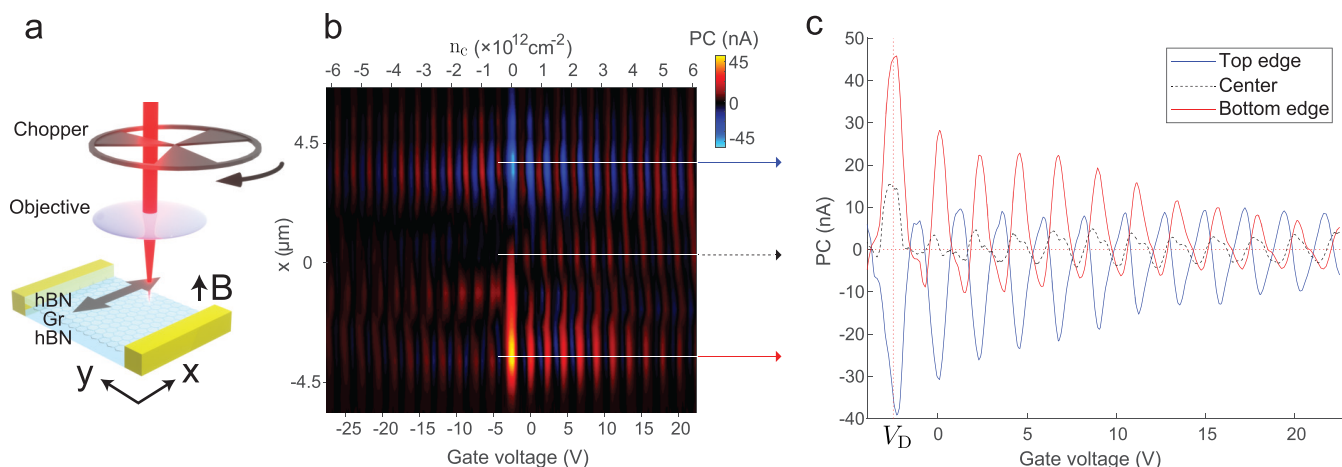
Figure 1. Schematics of the setup and the spatial profile of PC. (a) Schematics of the setup, illustrating that the PC is measured along the center line of the sample in the x direction (gray arrow) as a function of position and gate voltage. The PC is measured at $+B$ and $-B$. The PCs of two opposite fields are subtracted to isolate the contribution to the PC which depends on the orientation of the B-field, plotted in (b) for $B = 4.5$ T. The much weaker contribution which is independent from the orientation of B is shown in Figure S5 in the Supporting Information. (b) Measured PC as a function of the x position and gate voltage. Prominent PC oscillations are observed on the edges (located at $x = \pm 4.5\ \mu$m), whereas the PC is minimal in the bulk (located around $x = 0\ \mu$m). This indicates that the PC is predominately attributed to the edge states. (c) Cuts of the PC on the edges as a function of gate voltage. The zeros of the PC at high LLs match with the even fillings (ignoring spin) of the LLs (systematically shown in Figure 2a). PC oscillations on the two edges have opposite polarities, indicating that the PC is related to the chiral transport of carriers on the edges.

evidence of CM in a Landau quantized monolayer graphene using electric measurements is still ambiguous.[16,25,26] Experimentally, PC measurements from graphene in the quantum Hall regime are commonly obscured by the sample's substantially varying impedance when sweeping the Fermi level through many LLs. In addition, spatial scans of PC can be correlated with inhomogenous doping and charge puddles.[9] These make the analysis of the PC mechanism even more challenging.

Here, we address these technical challenges by using a trans-impedance amplifier (TIA). This allows an accurate and precise measurement of PC, independent of the sample's varying impedance,[27−29] while simultaneously keeping other parameters strictly controlled. At fixed magnetic fields, we observe prominent PC oscillations with opposite polarities on each of the two edges of the sample, as the Fermi level is swept through LLs. On top of these oscillations, our measurement technique reveals a rich additional structure of the PC, which provides clear insight into the microscopic processes which are at work when generating the out-of-equilibrium currents. These details include an envelope curve of the oscillations (especially in weak magnetic fields), a nonsinusoidal shape of the oscillations (especially in strong magnetic fields), as well as a characteristic dip of the PC at the Dirac point. In addition, we find the PC saturates with optical intensity and the critical power of this saturation changes as the Fermi level sweeps through LLs. By applying a model using optical Bloch equations to simulate the PC, and by matching the model data the observed PC, we obtain crucial hints related to the carrier relaxation in graphene. Specifically, our quantitative model of the non-equilibrium dynamics contains the scattering of excited carriers with acoustic and optical phonons, as well as Coulomb carrier−carrier interactions. The PC is then calculated based on hot carrier populations and their edge chiralities (group velocities) arising from energy dispersions on the edges. Agreement between experiment and model does not only confirm the qualitative picture based on a relaxation

bottleneck, but it also provides compelling evidence of CM. The simulation indicates that the PC oscillation is due to the alternating balance of available number of states for electrons and holes as we sweep the Fermi level through quantized LLs. As carriers relax across the Dirac point, the PC contributions from electrons and holes change from constructive to destructive, explaining the observed pattern of critical saturation powers. In addition, we find that the simulated PC matches the measurement at high magnetic fields only when Coulomb scattering is included, revealing evidence for CM. Our work provides a study of carrier relaxation processes using continuous excitation, which extends beyond the ultrafast regime studied in most pump−probe measurements. In addition, our evidence of the long-coveted electrically measured CM will contribute to applications of graphene as efficient light detection devices. Finally, based on our model, PC may be used to explore additional topological phenomena in the emerging fields of 2D materials and twistronics.[30,31]

RESULTS AND DISCUSSION

Experimental Observations. The experimental setup is shown in Figure 1a. We focus a stabilized weak continuous-wave (CW) laser (<10 μW, $\lambda = 940$ nm) on a two-terminal square sample with dimensions (∼10 μm) much larger than the laser spot (∼1 μm). The sample is at a temperature ∼4 K and has a mobility of 13100 cm^2/(Vs). The laser is chopped by a mechanical chopper with a frequency ∼300 Hz. We move the laser spot position on the sample and record the PC as a function of the gate voltage through two electrical contacts. The sample is not biased by any external voltage. The PC is measured via a homemade TIA which converts current to voltage independent of the sample's substantially varying impedance when sweeping the Fermi level through many LLs. This guarantees accurate measurements of the PC, including the corresponding current amplitude envelopes (see Supporting Information for discussions) as well as minimizes the Johnson−Nyquist noise from the sample.[29] The voltage output
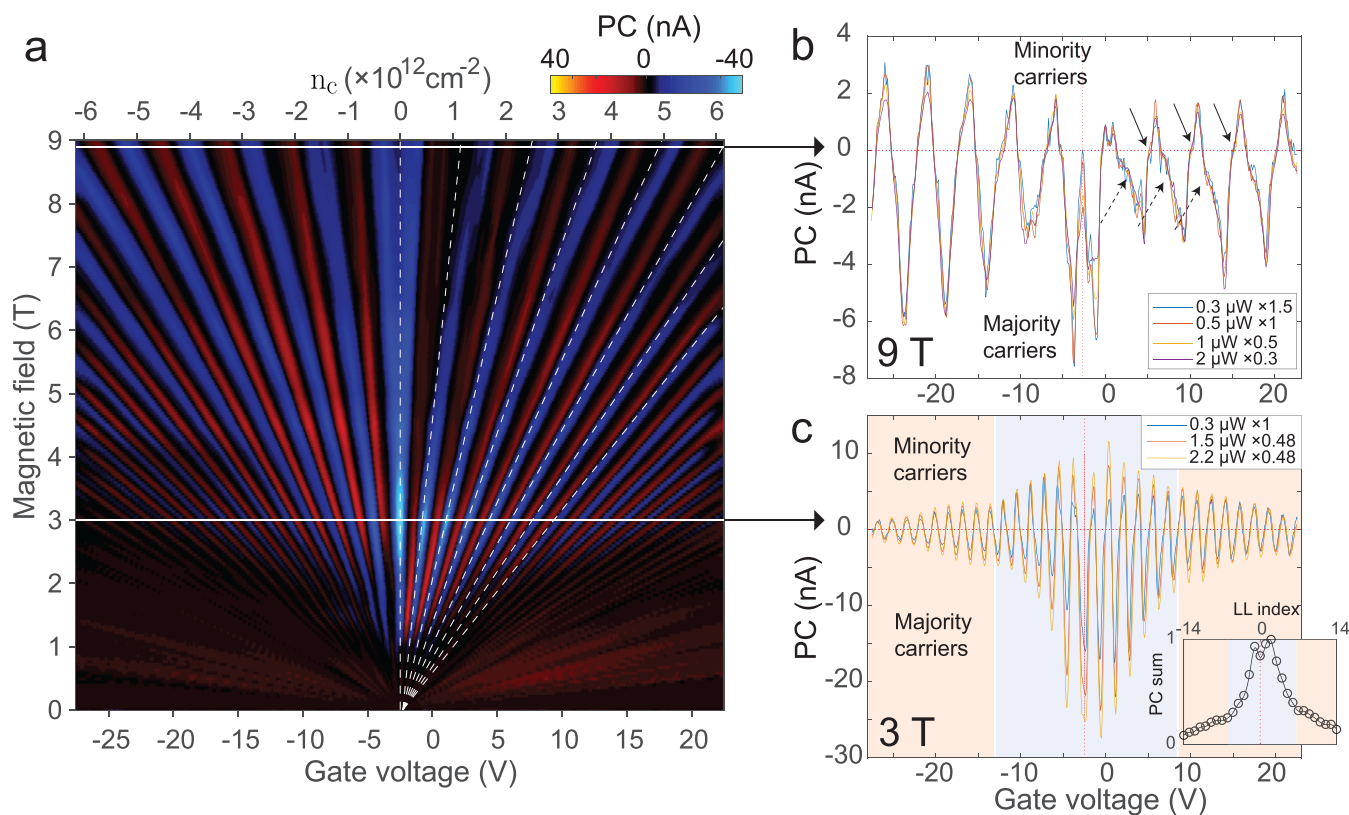
Figure 2. Magnetic field dependence of the PC on the edge. (a) PC on the top sample edge as a function of field strength and gate voltage is plotted, showing the Landau fan for the PC. The excitation power used is 1 μW. Data for 0.3 and 2 μW are shown in Figure S6 in the Supporting Information. The dashed white lines are even fillings of LLs (ignoring spin) extracted from the transport fan (see Figure S2 in the Supporting Information). As E_F is scanned, each LL (except the 0th) gives rise to a positive and a negative PC peak. (b) Cuts of PC for various pump powers at a high field of 9 T, scaled by factors given in the legend. The shape of the oscillations shows that polarity changes at even fillings (dashed black arrows) are smoother than those at odd fillings (solid black arrows). We also see a prominent dip at the Dirac point which is due to efficient carrier relaxation when E_F = 0. (c) Cuts of the PC (scaled vertically by factors shown in the legend) for various pump powers at a low field of 3 T. Based on measurements and simulations, the side with a more substantial envelope (the negative side) is attributed to the majority carriers and the other (the positive side) to the minority carriers, as marked in (b,c). The scaled PC cuts overlap well for high LLs but not near the Dirac point, indicating inhomogeneous PC power dependence with respect to LLs. In addition, we sum over the absolute values of the two PC peaks originating from the same LL and plot as a function of LL index in the inset of (c). The plot shows two regimes shaded in yellow and blue, where the blue regime has larger slopes than the yellow, indicating different mechanisms, consistent with our model. Error bars are smaller than markers. Measurements on the other sample, showing the same behaviors, are given in the Supporting Information.

of the TIA is measured with a lock-in amplifier which is frequency-locked with the chopped laser. Our measurements are repeated on two samples (see Supporting Information).

First, we spatially map the PC on the sample at a fixed magnetic field, as illustrated in Figure 1a with experimental data in Figure 1b. Specifically, we stabilize the laser spot at a fixed position on the center line of the sample and record the PC as a function of the gate voltage. Then we scan the laser spot position from edge to edge along the perpendicular center line to obtain a two-dimensional plot (vs *x* and gate voltage). We find that the strength and polarity of the PC depend on the position of the laser, as we scan the laser spot across the sample, along the center line, as shown in Figure 1a, and the gate voltage, controlling the Fermi level (E_F) in the sample. We have determined that the PC is independent of the laser polarization. Thus, we ignore the spin degree of freedom and define even fillings as E_F in the middle of LLs, whereas odd fillings as in the middle of LL gaps. Next, we reverse the magnetic field, and we find that the PC signals are approximately reversed as well, especially when the laser spot is close to a sample edge. Therefore, we subtract the scans for

+*B* and −*B* to separate the PC contribution which is dependent on the orientation of *B* ("orientation-dependent PC") from the one which is independent from the orientation of the *B*-field. The orientation-dependent PC is plotted in Figure 1b as a function of laser spot position and the gate voltage. The much weaker orientation-independent PC, caused by direct diffusion,[32] is shown in Figure S5 in the Supporting Information. In Figure 1c, we further visualize our data by showing cuts of the orientation-dependent PC as a function of gate voltage at three different positions on the sample: top edge, bottom edge, center. These plots highlight various features of the PC measurement: First, the orientation-dependent PC is strongly enhanced at the edges. Second, the PC oscillates with the gate voltage, and is strongest at the edges. Third, opposite edges give PC oscillations with opposite polarities. Fourth, PC peak values decrease as the backgate voltage increases away from the Dirac point.

We repeat our measurement on the top edge at different magnetic field strength up to 9 T. We find that the PC exhibits a Landau fan, shown in Figure 2a. Notably, this fan closely resembles the fan seen in conventional transport measure-
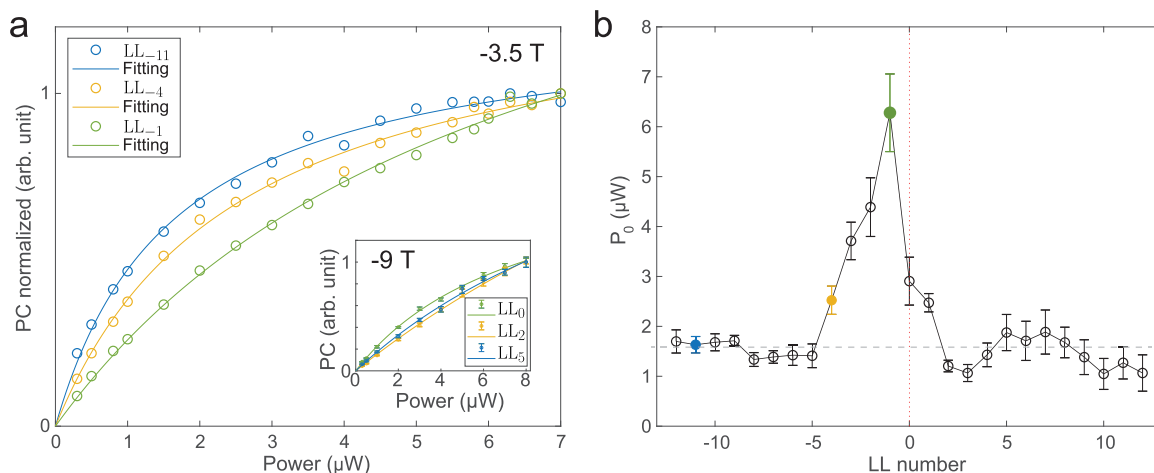
Figure 3. Power saturation behaviors of PC at various LLs. (a) Normalized PC at various LLs on the majority carriers side, as a function of optical power at 3.5 T. We observe little sign of PC saturation for LL$_{-1}$, while for LLs with larger indices (LL$_{-4}$ and LL$_{-11}$), the PC is saturated more easily. The largest contribution to this effect is the carriers (electrons and holes) from above or below the Dirac point. At high LLs, the PC is proportional to the *subtraction* of hot electrons and hole populations, which is limited by the relaxation rates difference (relaxation bottleneck). In contrast, for the low LLs, the PC is given as a *sum* over the populations of the two. In comparison, at a higher field of 9 T, there is little sign of saturation as shown in the inset. The error bars in (a) are smaller than the markers. (b) Fitted saturation powers P_0 of the data shown in (a) as a function of the corresponding LL index. For high LLs, P_0 remains flat (gray dashed line as a guide for the eyes) which is a result of the relaxation bottlenecks for E_F at different high LLs saturated at the same power. The error bars represent 95% confidence of fittings.
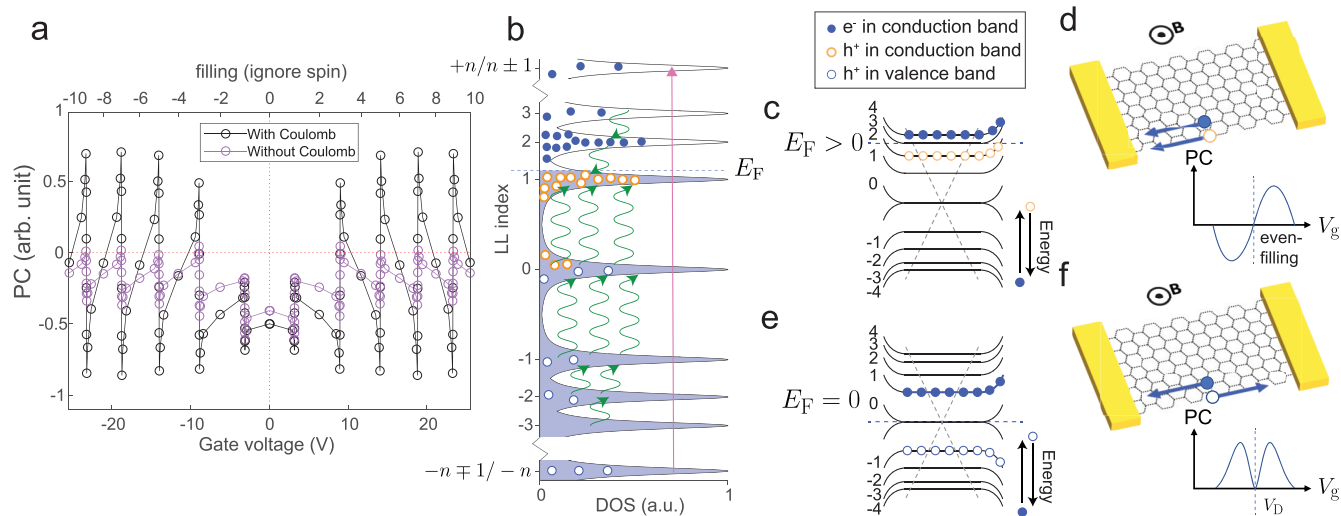

Figure 4. Modeling and simulations of the PC. (a) Simulated PC with and without Coulomb interactions as a function of gate voltage. The simulated PC with Coulomb interactions match the measured PC at 9 T shown in Figure 2b, whereas the simulation without Coulomb interactions does not, showing the importance of contributions from Coulomb interactions in the PC. In particular, without a Coulomb interaction, the simulated PC decreases with gate voltage away from the Dirac point, whereas the opposite trend appears for the case with Coulomb, which matches with the observation in Figure 2b. In addition, the simulations with Coulomb interactions have asymmetries between the positive and negative PC peaks away from the Dirac point that match well with the data represented in Figure 2b, whereas the simulations without Coulomb interactions do not. Moreover, the asymmetric LL PC peak shape also matches the observations (see arrows in Figure 2b). (b) Illustration of the excitation and carrier relaxations across LLs. Selection rules allow optical excitations of carriers between LLs $-n$ and $n \pm 1$, $-n \pm 1$, and n. Depending on E_F, excited electrons and holes may relax to the same side of the Dirac point. These electrons and holes share the same edge chirality (e.g., the holes above the Dirac point, orange hollow circles, and the electrons, blue solid dots) and therefore give rise to the destructive part of the PC. (c,d) Illustrations of electrons and holes on the same side of the Dirac point having the same edge chirality, giving a destructive PC. (e,f) Illustrations of electrons and holes on different sides of the Dirac point having opposite edge chiralities, giving a constructive PC.

ments (transport measurements are plotted in the Supporting Information). Additional features of the PC measurement are revealed by comparing PC slices at different fields, e.g., at 9 and 3 T as shown in Figure 2b,c for various laser intensities, where each PC slice is scaled vertically such that all of the slices overlap at large backgate voltages. At low field (Figure

2c), the PC peaks form an envelope with larger PC values closer to the Dirac point, while the envelop diminishes at high field (Figure 2b). The envelope at low field can be separated into two regimes, with different slopes of PC as a function of gate voltage. This is highlighted in the inset of Figure 2c, where we sum over the absolute value of two PC peaks (positive and

negative) arising from the same LL and plot as a function of LL index. The positive PC values are due to minority carriers (i.e., electrons in the valence band or holes in the conduction band), whereas the negative PC values are due to majority carriers (i.e., holes in the valence band or electrons in the conduction band), indicated on the left of Figure 2c. This is discussed below.

Finally, we study the PC amplitude dependence on the laser intensity. By comparing the maximum PC amplitudes (negative PC values in Figure 2c, which is due to majority carriers) at various LLs with different laser intensity, shown in Figure 3a, we find that when the magnetic field is low, the PC exhibits only weak saturation when the Fermi level is near the Dirac point. But when the Fermi level is away from the Dirac point (above $LL_{\pm 5}$), the PC saturates at a constant laser power as shown in Figure 3b. The saturation powers P_0 are fitted with the saturable absorber model:[33,34]

$$J \propto \frac{P/P_0}{1 + P/P_0} \tag{1}$$

The extracted P_0 corresponding to LL_{-12} to LL_{+12} is plotted in Figure 3b.

Theoretical Model. In order to model our data, we first recall that quantum Hall systems are insulating in the bulk, but have B dependent chiral transport on the edge when E_F is within a LL gap. Therefore, we assume that the PC part which depends on the orientation of B is given by intralevel currents from the system edge. We denote the carrier population by $n_{\nu,k}$ where ν is the LL index, and k is the wavenumber. The population shall refer to electrons above the Fermi level and to holes below the Fermi level. The PC generated by excited carriers is given by $J \sim \sum_\nu \int dk q_\nu v_{\nu,k} k n_{\nu,k}$, where $v_{\nu,k}$ is the group velocity of the given level, and q_ν takes into account the charge of the carrier: $q_\nu = 1$ when ν is below the Fermi level; $q_\nu = -1$ when ν is above the Fermi level. Specifically, $q_\nu = 0$ when ν is at the Fermi level (i.e., for carriers within the LL where the Fermi level is located) accounts for the existence of both electrons and holes in the vicinity of the Fermi level, as well as for the divergent phonon coupling strength, where the divergent acoustic phonon coupling strength $\propto 1/\omega$ in the limit of small frequencies.[20] To simplify the situation, we assume a constant group velocity $v_{\nu,k} = v_\nu$, whose precise value depends on the position of the laser spot on the sample. With this simplification, the current will be determined by the average population of the LL, $n_\nu \sim \int dk n_{\nu,k}$. Due to opposite velocities on the two edges, v_ν changes sign as the laser is moved from one edge to the opposite edge, explaining the PC polarity flip from edge to edge shown in Figure 1b.

At a fixed laser position, due to opposite edge chirality of LLs ν and $-\nu$, the velocities take opposite values: $v_\nu = -v_{-\nu}$, as illustrated in Figure 4e,f. In view of the otherwise identical transport properties in LLs, we take the group velocity to be a constant, i.e., $|v_\nu| = v$.[35,36] An exception from this occurs when $\nu = 0$ (LL_0), where the lack of well-defined edge chirality yields $v_0 = 0$ due to non-equilibrium distributions.[11,12] With these simplifications, the PC signal is

$$J \sim v \sum_{\nu \neq 0} q_\nu \text{sign}(\nu) n_\nu$$

This is similar to the Shockley−Ramo theorem[37,38] except that here the group velocities are given by the edge chirality rather than an electric field.

To determine the average LL population n_ν, we employ the optical Bloch equations, as described in details in the Methods section. They determine the steady state in the presence of optical excitation and different relaxation channels (acoustic phonons, optical phonons, Coulomb scatterings). The result of our PC simulation is shown in Figure 4a. In particular, our PC model reproduces the PC oscillations as a function of gate voltage seen in the experiment. With all relaxation channels considered, the envelope of the simulated current matches with the experimentally obtained envelope in the high field regime. This is understood as certain assumptions in our simulation implicitly assume a strong magnetic field. Specifically, we neglected mixing between LLs, and the number of LLs in the simulation was limited to 21, which is close to the resolvable number of LLs (see Methods).

Discussion. The part of PC which depends on the orientation of the B-field is dominated by carriers at the edge (see Figure 1b). If all carriers on the edge contribute equally to the PC, the measured PC should not oscillate. To explain the prominent PC oscillations on the edge, we develop an effective model where the PC is due to the hot carriers whereas the carriers near E_F have little contribution due to the divergent acoustic phonon coupling strength between electrons and holes at E_F which has been elaborated above.

The polarity of edge current has two contributions. First, it depends on the chirality of the particular edge state,[9] which is incorporated in our theoretical model through the opposite group velocities for LLs above and below the Dirac point, as shown in Figure 4c−f. Second, the current polarity also depends on the charge of the hot carrier. Thus, if the Fermi level is sufficiently far away from the Dirac point, all hot carriers in the vicinity of the Fermi level will be on the same side of the Dirac point and contribute to the PC with the same edge chirality.[39,40] However, electrons and holes contribute with opposite charges, therefore, in this case the PC signal reflects a mismatch (a subtraction) between the number of hot electron carriers and hole carriers. The magnitude of this mismatch crucially depends on the position of the Fermi energy within the LL. More specifically, as we sweep E_F through a LL, the available number of states for electrons and holes alternates (illustrated in Figure 4b), generating unbalanced carrier numbers in accordance with Fermi's golden rule. This mechanism pictorially explains the PC oscillations (cf. also ref 9) which are also reproduced by our microscopic quantitative model invoking the relaxation of carriers, with edge chirality after photoexcitation. Details of the oscillation asymmetries, oscillation envelop structure, and the shape of oscillations are discussed below in the context of our model.

In the low field case (see Figure 2c for instance), asymmetries in the absolute values of the maximum PC between the majority and minority side are present at lower backgate voltage, i.e., near the Dirac point. As the Fermi level nears the Dirac point, the occupation of chiral edge states both above and below the Dirac point must be considered. Without considering carrier type, edge states on opposite sides of the Dirac point have opposite chirality. Thus, if a carrier population extends across the Dirac point, populations of the same carrier type on each side of the Dirac point contribute to opposite PC directions. Therefore, hot carrier populations above the Dirac point will add constructively with opposite carrier types below the Dirac point and destructively with opposite carrier types on the same side of the Dirac point,[9] leading to asymmetries in the maxima of the absolute values of

PC oscillations (Figure 2c). In both the experimental data, Figures 1c and 2, and in the simulation data, Figure 4a, we observe this asymmetry between positive and negative PC peaks.

This asymmetry manifests differently in high and low magnetic fields. In the high field case, due to the larger LL gaps, there are less LLs for relaxation compared to the low field case. As a result, most of the relevant LLs have well-defined edge chiralities. Therefore, the asymmetry manifests as a constant offset to PC for all LLs, which is shown in both the simulation (Figure 4a) and measurements (Figure 2b). In the low magnetic field case, the excitation energy corresponds to LLs with much larger index. These high LLs are merged together (measurements shown in Figure S9 in the Supporting Information), and thus they do not have well-defined edge chirality due to the lack of gaps.[1] Therefore, in this case, the distribution of hot carriers only affects the PC peaks when E_F is in the low LLs and form the envelope as seen in Figure 2c, and it is elaborated next.

The concept of opposite carrier types on opposite sides of the Dirac point adding constructively to the PC reaches an extreme when the Fermi level is within the zeroth LL in the low field, again as shown in Figure 2c. With the Fermi level at the Dirac point, electrons necessarily belong to LLs above the Dirac point, whereas holes necessarily belong to LLs below the Dirac point. Together with the opposite edge chirality of electrons and holes regardless of their LL index, this leads to a situation in which their PC contributions are always constructive[14] and no polarity change can occur. Thus, in the low magnetic-field case, this situation gives rise to an envelop in the PC oscillation, in which the majority carrier side is peaking near the Dirac point. While when E_F moves away from the Dirac point, the constructive component is reduced as the distribution of hot carriers moves across the Dirac point. When E_F is far away from the Dirac point in this low magnetic field case, electrons and holes are mostly located on the same side of the Dirac point, so that electron and hole current contributions add destructively and the PC oscillations are almost symmetric. The two regimes: E_F near and away from the Dirac point, are indicated using different background shading colors in Figure 2c. In addition, in the inset in Figure 2c, we sum over the absolute values of PC peaks belonging to the same LL to highlight the different slopes of the PC amplitudes versus backgate voltage. The two regimes—one close to and one away from the Dirac point—are clear, reflecting our model.

When the field strength is high, an important caveat to our model is the fast relaxation of both types of carriers when E_F = 0. This results in a dip of the PC at the Dirac point and it is seen in the strong field data of Figure 2b and the simulation in Figure 4a. This dip in our data is not due to sublattice symmetry breaking from a Moiré pattern[41,42] or interaction-induced valley symmetry breaking of the LL_0,[13,43−45] since none of the corresponding features, such as the minibands and LL splittings, is observed in our transport measurements (see Figure S2 in the Supporting Information).

Using the PC envelopes, we see evidence for carrier multiplication.[19,23] Specifically, in Figure 2c, as we sweep E_F from high LLs to the Dirac point, the majority carrier PC peaks increase in amplitude, as a consequence of minority carriers starts to distribute across the Dirac point, which is discussed above. This alone is not an evidence of CM, but carrier distribution around the Dirac point. However, the minority carrier peaks grow as well and the only explanation of both the majority and minority carrier PC peaks increase in our model is that carriers are multiplied as they relax from high LLs to low LLs. This is also accompanied by simulations: by turning off the Coulomb interactions, simulations show much weaker PC, and the simulated envelope (Figure 4a) matches the measured one at high field (Figure 2b) only if Coulomb scattering is taken into account.

The unique shape of the individual oscillations within a LL is well-represented in our theoretical model and is strikingly similar to our high-magnetic field experimental data. This asymmetry in the individual oscillation shape gives insight into the hot-carrier relaxation process. In particular, when E_F sweeps pass the even filling point in a LL, hot carriers of one type slowly outnumber the other type, leading to a smooth PC polarity flip. In contrast, when the LL is gapped and E_F sweeps pass an odd filling point in the LL, the number of available states for relaxation quenches. This creates a relaxation bottleneck for one carrier type, whereas relaxation from the other carrier type emerges, leading to a shape change in PC. This is seen in the experimental data of Figure 2b, where the oscillations are clearly not sinusoidal. At positive gate voltage, we note that positive PC peaks are not aligned exactly in the middle of two negative PC peaks. Instead, they are shifted toward the Dirac point, which makes the PC polarity changes at odd fillings (marked by solid black arrows in Figure 2b) more abrupt than the ones at even fillings (marked by dashed black arrows in Figure 2b). This feature is matched in our simulation (Figure 4a).

Experimental data related to PC saturation are shown in Figure 3 and can provide additional insights to carrier distributions. We observe that the PC for low LLs does not saturate, whereas the high LL PC saturates much easier. This is consistent with our model since the PC for low LLs is mainly a sum of the electron and hole currents, whereas in the high LL regime, the PC saturates much easier since it is the difference of electron and hole currents and thus bottlenecked by the difference of relaxation rates of electrons and holes.[25,46] This is evidenced by the observed markedly different saturation powers, P_0 for low and high LL (Figure 3b) which supports the different mechanisms of the PC generation in these two regimes. In addition, in Figure 2c, we see the scaled PCs measured as a function of different laser powers overlap well in the high LLs but do not for the low ones, indicating inhomogeneous PC power dependence with respect to LLs.

CONCLUSIONS

In conclusion, we accurately measure the PC in graphene in the quantum Hall regime by using a TIA. The improved accuracy allows us to correlate particular experimental features with our theory and simulations to form a coherent model of PC in the quantum Hall system. In particular, the balance between hot electrons and hot holes oscillates with the alternating available number of states for electrons and holes near the Fermi level, as it is swept through LLs. The chiral current contributions from these hot carriers are determined by the edge chirality of carriers originated from the confinement dispersion, together with their charge. As a consequence of the flipped edge chirality across the Dirac point as well as a hot carrier distribution over LLs, PC shows different saturation behaviors when the Fermi level is close or away from the Dirac point. In addition, inclusion of the carrier multiplication and Coulomb interaction is imperative to

explain the simultaneously growing majority and minority carrier PC peaks in the low field and the PC oscillation pattern in the high field.

We believe our coherent model of PC from graphene in the quantum Hall regime will push the development of applications using graphene such as single-photon detection[47−49] and light harvesting,[50,51] as an electrically measured CM has been long-coveted.[25] Novel quantum Hall regimes, with modified optical properties, can be realized with a giant synthetic gauge field.[52] Our findings will also facilitate exploring additional physics such as studies of twistronics.[53] In this context, an interesting application of PC measurements are the different Chern insulating phases,[30,31] characterized by different nonzero Chern numbers. Although Chern numbers are defined by the linear response of the system, it can be expected that also the PC, as a far-from-equilibrium probe, carries some signatures of the topological index—to some extent similar to the chirality trace discussed in the present article. Moreover, photocurrent measurements might prove useful to investigate extended states in topological quantum devices by using twisted light.[54] In addition, they may provide a different angle for studying and distinguishing topological edge currents[55−57] and the recently confirmed nontopological edge currents.[58,59] Finally, another interesting application could be the control of the CM.[60]

METHODS

Sample Fabrication. Graphene was exfoliated from natural graphite crystals (HQ Graphene) and hBN was exfoliated from a synthetic crystal.[61] Both materials were exfoliated using the Scotch-tape method on two different Si substrates with a dry-grown 90 nm thick SiO$_2$ layer on top. Monolayer graphene and 10−15 nm thick hBN were identified based on the color contrast on their respective substrates by an optical microscope. Thicknesses of each material were later confirmed by micro-Raman[62] and atomic force microscopy. Heterostructures of hBN/graphene/hBN were assembled by a hot pick-up method[63] on the same type of substrates. The backside of the substrates was metallized and used as a backgate. Assembled heterostructures were shaped into squares of different sizes, ranging from 3 μm × 3 μm to 10 μm × 10 μm, by electron-beam (e-beam) lithography. The heterostructures were etched by reactive-ion etching (RIE) employing an 80 nm thick Al hard mask deposited in an e-beam evaporator. Graphene and hBN were etched selectively by O$_2$ and SF$_6$ plasma, respectively, to expose edges of graphene. The hard mask was removed in tetramethylammonium hydroxide solution after etching. The graphene edges were exposed along all four sides of the square-shaped heterostructures. Two of the graphene edges exposed on the opposite sides of the square were metallized to realize electrical contacts.[64] The Cr/Pd/Au (2/5/80 nm) contacts were patterned by e-beam lithography and slightly overlapped the heterostructures. They were deposited in an e-beam evaporator at the base pressure of 10^{-6} mbar. Fabricated devices were wire-bonded to chip carriers for the electrical and PC measurements.

Transport and PC Measurements. Standard transport measurements are obtained with low frequency lock-in technique with an excitation current of 20 nA at 13 Hz. Each transport data point is an average of 10 measurements. Gate voltage sweeping is achieved using a DC source measure unit (Keithley 2400). The gate voltage is ramped with a step size of 5 mV, and between two steps, a wait time of 10 ms is added to avoid hysteresis. Every 10 steps, we wait another 200 ms. The sample resistance is measured every 20 or 100 mV depending on the total scan range of gate voltage. PC measurements are obtained with a chopped laser at 308 Hz. The intensity, polarization, and wavelength of the laser are stabilized at a frequency of 30 Hz to ensure accurate measurements. Further information are given in the Supporting Information. The sample, inside a variable temperature insert (VTI), is mounted on top of a piezo-electric stack

(scanners (ANSxy100) and positioners (ANPx101, ANPz201), with a total resolution of sub-nanometers). It is cooled down to 4 K, and an out-of-plane magnetic field up to 9 T can be applied. The VTI has an optical window on top and a confocal microscope is built above to optically resolve the sample. The excitation laser is illuminated through the same window and the laser spot's position with respect to the sample can be monitored with the microscope and can be adjusted with the stack as well as a piezo-controlled mirror mount. The sample is not biased. The two electrodes of the sample are connected to the TIA located outside the cryostat and the outputs of the TIA are connected with the frequncy-locked lock-in amplifier (SR860). Each data point of the PC is an average of 10 measurements. Details of the TIA can be found in the Supporting Information.

Optical Bloch Equations. For a theoretical description of the system dynamics, we employ optical Bloch equations for Landau quantized graphene.[19,20,54] The population of LL$_i$ (averaged over all orbitals) is denoted by ρ_i, and the (averaged) polarization between two LLs is denoted by P_{ij}. Their equations of motion read as follows:

$$\dot{\rho}_i = 2\text{sign}(i)\text{Re}(\Omega_{ij}P_{ij}) + S_i^{(\text{in})}(1 - \rho_i) - S_i^{(\text{out})}\rho_i \tag{2}$$

$$\dot{P}_{ij} = -\Omega_{ij}^*(\rho_i - \rho_j) - \frac{\Gamma_0}{\hbar}P_{ij} \tag{3}$$

Here, we choose the rotating frame of the light field, in which we further employ the rotating wave approximation. With this, the Rabi frequency Ω_{ij} takes nonzero values Ω_0 only for two resonant pairs of Landau levels, $(i, j) = (n_{\text{min}}, n_{\text{max}} - 1)$ and $(i, j) = (n_{\text{min}} + 1, n_{\text{max}})$. For the modeling, we assume $n_{\text{min}} = -10$ and $n_{\text{max}} = 10$. This is because that the number of resolvable LLs in the sample #2065 is ~29, and this number does not change with B,[65] and we limit the total number of LLs to 21 due to computational cost. Choosing the electromagnetic vector potential for the light field at a constant value $A = 5 \times 10^{-10}$ Vs/m, the Rabi frequency is given by $\Omega_0 = \frac{e}{m_e}M_{if}A = 200$ GHz, with an optical matrix element between nonzero Landau levels $M_{if} = 2.25 \times 10^9$ m^{-1}.[20] The scattering terms $S_i^{(\text{in})}$ and $S_i^{(\text{out})}$ are given in the Supporting Information. The effect of scattering on the polarization is accounted by the dephasing Γ_0, combined with the scattering at impurities which are responsible for Landau level broadening. We take Γ_0 as a phenomenological quantity, which roughly can be chosen in a range between $\Gamma_0 = 5−10$ meV to achieve good matches.

ASSOCIATED CONTENT

Ⓢ Supporting Information

The Supporting Information is available free of charge at https://pubs.acs.org/doi/10.1021/acsnano.2c05502.

Calculation of scattering rates and pseudopotentials, experimental details of transport and PC measurements, and additional data (PDF)

AUTHOR INFORMATION

Corresponding Authors

Mohammad Hafezi − *Joint Quantum Institute, NIST/ University of Maryland, College Park, Maryland 20742, United States; IREAP, University of Maryland, College Park, Maryland 20742, United States;* Email: hafezi@umd.edu

Glenn S. Solomon − *Joint Quantum Institute, NIST/ University of Maryland, College Park, Maryland 20742, United States; Department of Physics and IPAS, University of Adelaide, Adelaide, South Australia 5005, Australia;* ⓞ orcid.org/0000-0002-1920-2564; Email: glenn.solomon@adelaide.edu.au

Authors

Bin Cao − *Joint Quantum Institute, NIST/University of Maryland, College Park, Maryland 20742, United States;* orcid.org/0000-0002-1162-8843

Tobias Grass − *Joint Quantum Institute, NIST/University of Maryland, College Park, Maryland 20742, United States; ICFO-Institut de Ciencies Fotoniques, The Barcelona Institute of Science and Technology, Barcelona 08860, Spain; DIPC—Donostia International Physics Center, San Sebastian 20018, Spain; Ikerbasque—Basque Foundation for Science, Bilbao 48013, Spain*

Olivier Gazzano − *Joint Quantum Institute, NIST/University of Maryland, College Park, Maryland 20742, United States; Present Address: ONERA—The French Aerospace Lab, Palaiseau, France*

Kishan Ashokbhai Patel − *L-NESS, Department of Physics, Politecnico di Milano, 22100 Como, Italy*

Jiuning Hu − *National Institute of Standards and Technology, Gaithersburg, Maryland 20878, United States*

Markus Müller − *Joint Quantum Institute, NIST/University of Maryland, College Park, Maryland 20742, United States*

Tobias Huber-Loyola − *Joint Quantum Institute, NIST/University of Maryland, College Park, Maryland 20742, United States*

Luca Anzi − *L-NESS, Department of Physics, Politecnico di Milano, 22100 Como, Italy*

Kenji Watanabe − *National Institute for Materials Science, 305-0044 Tsukuba, Japan;* orcid.org/0000-0003-3701-8119

Takashi Taniguchi − *National Institute for Materials Science, 305-0044 Tsukuba, Japan;* orcid.org/0000-0002-1467-3105

David B. Newell − *National Institute of Standards and Technology, Gaithersburg, Maryland 20878, United States*

Michael Gullans − *Joint Center for Quantum Information and Computer Science, NIST/University of Maryland, College Park, Maryland 20742, United States*

Roman Sordan − *L-NESS, Department of Physics, Politecnico di Milano, 22100 Como, Italy;* orcid.org/0000-0001-7373-0643

Complete contact information is available at:
https://pubs.acs.org/10.1021/acsnano.2c05502

Author Contributions

△B.C. and T.G. contributed equally to this work.

Notes

The authors declare no competing financial interest.

REFERENCES

(1) Hasan, M. Z.; Kane, C. L. Colloquium: topological insulators. *Reviews of modern physics* **2010**, *82*, 3045.

(2) Qi, X.-L.; Zhang, S.-C. Topological insulators and superconductors. *Rev. Mod. Phys.* **2011**, *83*, 1057.

(3) Halperin, B. I. Quantized Hall conductance, current-carrying edge states, and the existence of extended states in a two-dimensional disordered potential. *Phys. Rev. B* **1982**, *25*, 2185.

(4) Jackiw, R.; Rebbi, C. Solitons with fermion number 1/2. *Physical Review D* **1976**, *13*, 3398.

(5) Girvin, S. M.*Topological Aspects of Low Dimensional Systems*; Springer: Berlin, 1999; pp 53−175.

(6) Patlatiuk, T.; Scheller, C. P.; Hill, D.; Tserkovnyak, Y.; Barak, G.; Yacoby, A.; Pfeiffer, L. N.; West, K. W.; Zumbühl, D. M. Evolution of the quantum Hall bulk spectrum into chiral edge states. *Nat. Commun.* **2018**, *9*, 3692.

(7) Williams, J.; DiCarlo, L.; Marcus, C. Quantum Hall effect in a gate-controlled pn junction of graphene. *Science* **2007**, *317*, 638−641.

(8) Abanin, D.; Levitov, L. Quantized transport in graphene pn junctions in a magnetic field. *Science* **2007**, *317*, 641−643.

(9) Nazin, G.; Zhang, Y.; Zhang, L.; Sutter, E.; Sutter, P. Visualization of charge transport through Landau levels in graphene. *Nat. Phys.* **2010**, *6*, 870−874.

(10) Queisser, F.; Schützhold, R. Strong magnetophotoelectric effect in folded graphene. *Physical review letters* **2013**, *111*, 046601.

(11) Abanin, D. A.; Lee, P. A.; Levitov, L. S. Charge and spin transport at the quantum Hall edge of graphene. *Solid state communications* **2007**, *143*, 77−85.

(12) Abanin, D. A.; Novoselov, K. S.; Zeitler, U.; Lee, P. A.; Geim, A. K.; Levitov, L. S. Dissipative quantum Hall effect in graphene near the Dirac point. *Physical review letters* **2007**, *98*, 196806.

(13) Kim, S.; Schwenk, J.; Walkup, D.; Zeng, Y.; Ghahari, F.; Le, S. T.; Slot, M. R.; Berwanger, J.; Blankenship, S. R.; Watanabe, K.; et al. Edge channels of broken-symmetry quantum Hall states in graphene visualized by atomic force microscopy. *Nat. Commun.* **2021**, *12*, 2852.

(14) Sonntag, J.; Kurzmann, A.; Geller, M.; Queisser, F.; Lorke, A.; Schützhold, R. Giant magneto-photoelectric effect in suspended graphene. *New J. Phys.* **2017**, *19*, 063028.

(15) Cao, H.; Aivazian, G.; Fei, Z.; Ross, J.; Cobden, D. H.; Xu, X. Photo-Nernst current in graphene. *Nat. Phys.* **2016**, *12*, 236−239.

(16) Wu, S.; Wang, L.; Lai, Y.; Shan, W.-Y.; Aivazian, G.; Zhang, X.; Taniguchi, T.; Watanabe, K.; Xiao, D.; Dean, C.; et al. Multiple hot-carrier collection in photo-excited graphene Moiré superlattices. *Science advances* **2016**, *2*, No. e1600002.

(17) Gazzano, O.; Cao, B.; Hu, J.; Huber, T.; Grass, T.; Gullans, M.; Newell, D.; Hafezi, M.; Solomon, G. S. Observation of chiral photocurrent transport in the quantum Hall regime in graphene. *arXiv* **2019**, DOI: 10.48550/arXiv.1903.01487.

(18) Wu, S.Device Physics of Two-Dimensional Crystalline Materials. Ph.D. Thesis, University of Washington, Seattle, 2016.

(19) Wendler, F.; Knorr, A.; Malic, E. Carrier multiplication in graphene under Landau quantization. *Nat. Commun.* **2014**, *5*, 3703.

(20) Wendler, F.; Knorr, A.; Malic, E. Ultrafast carrier dynamics in Landau-quantized graphene. *Nanophotonics* **2015**, *4*, 224−249.

(21) Song, J. C.; Tielrooij, K. J.; Koppens, F. H.; Levitov, L. S. Photoexcited carrier dynamics and impact-excitation cascade in graphene. *Phys. Rev. B* **2013**, *87*, 155429.

(22) Tielrooij, K. J.; Song, J. C. W.; Jensen, S. A.; Centeno, A.; Pesquera, A.; Zurutuza Elorza, A.; Bonn, M.; Levitov, L. S.; Koppens, F. H. L. Photoexcitation cascade and multiple hot-carrier generation in graphene. *Nat. Phys.* **2013**, *9*, 248−252.

(23) Mittendorff, M.; Wendler, F.; Malic, E.; Knorr, A.; Orlita, M.; Potemski, M.; Berger, C.; De Heer, W. A.; Schneider, H.; Helm, M.; et al. Carrier dynamics in Landau-quantized graphene featuring strong Auger scattering. *Nat. Phys.* **2015**, *11*, 75−81.

(24) Plotzing, T.; Winzer, T.; Malic, E.; Neumaier, D.; Knorr, A.; Kurz, H. Experimental verification of carrier multiplication in graphene. *Nano Lett.* **2014**, *14*, 5371−5375.

(25) Massicotte, M.; Soavi, G.; Principi, A.; Tielrooij, K.-J. Hot carriers in graphene−fundamentals and applications. *Nanoscale* **2021**, *13*, 8376−8411.

(26) Gierz, I.; Petersen, J. C.; Mitrano, M.; Cacho, C.; Turcu, I. E.; Springate, E.; Stöhr, A.; Köhler, A.; Starke, U.; Cavalleri, A. Snapshots of non-equilibrium Dirac carrier distributions in graphene. *Nature materials* **2013**, *12*, 1119−1124.

(27) Horowitz, P.; Hill, W.*The Art of Electronics*; Cambridge University Press: Cambridge, 2002.

(28) McIver, J. W.; Schulte, B.; Stein, F.-U.; Matsuyama, T.; Jotzu, G.; Meier, G.; Cavalleri, A. Light-induced anomalous Hall effect in graphene. *Nat. Phys.* **2020**, *16*, 38−41.

(29) Donati, S.*Photodetectors: Devices, Circuits and Applications*; John Wiley & Sons: Hoboken, NJ, 2021.

(30) Song, Z.; Wang, Z.; Shi, W.; Li, G.; Fang, C.; Bernevig, B. A. All Magic Angles in Twisted Bilayer Graphene are Topological. *Phys. Rev. Lett.* **2019**, *123*, 036401.

(31) Nuckolls, K. P.; Oh, M.; Wong, D.; Lian, B.; Watanabe, K.; Taniguchi, T.; Bernevig, B. A.; Yazdani, A. Strongly correlated Chern insulators in magic-angle twisted bilayer graphene. *Nature* **2020**, *588*, 610−615.

(32) Song, J. C.; Levitov, L. S. Shockley-Ramo theorem and long-range photocurrent response in gapless materials. *Phys. Rev. B* **2014**, *90*, 075415.

(33) Winzer, T.; Mittendorff, M.; Winnerl, S.; Mittenzwey, H.; Jago, R.; Helm, M.; Malic, E.; Knorr, A. Unconventional double-bended saturation of carrier occupation in optically excited graphene due to many-particle interactions. *Nat. Commun.* **2017**, *8*, 15042.

(34) Shen, Y.-R.*The Principles of Nonlinear Optics*; Wiley & Sons: Hoboken, NJ, 1984.

(35) Sonntag, J.; Reichardt, S.; Wirtz, L.; Beschoten, B.; Katsnelson, M. I.; Libisch, F.; Stampfer, C. Impact of many-body effects on Landau levels in graphene. *Physical review letters* **2018**, *120*, 187701.

(36) Abanin, D. A.; Lee, P. A.; Levitov, L. S. Spin-filtered edge states and quantum Hall effect in graphene. *Physical review letters* **2006**, *96*, 176803.

(37) Shockley, W. Currents to conductors induced by a moving point charge. *Journal of applied physics* **1938**, *9*, 635−636.

(38) Ramo, S. Currents induced by electron motion. *Proceedings of the IRE* **1939**, *27*, 584−585.

(39) Lee, G.-H.; Huang, K.-F.; Efetov, D. K.; Wei, D. S.; Hart, S.; Taniguchi, T.; Watanabe, K.; Yacoby, A.; Kim, P. Inducing superconducting correlation in quantum Hall edge states. *Nat. Phys.* **2017**, *13*, 693−698.

(40) Ben Shalom, M.; Zhu, M. J.; Fal'ko, V. I.; Mishchenko, A.; Kretinin, A. V.; Novoselov, K. S.; Woods, C. R.; Watanabe, K.; Taniguchi, T.; Geim, A. K.; Prance, J. R.; et al. Quantum oscillations of the critical current and high-field superconducting proximity in ballistic graphene. *Nat. Phys.* **2016**, *12*, 318−322.

(41) Hunt, B.; Sanchez-Yamagishi, J. D.; Young, A. F.; Yankowitz, M.; LeRoy, B. J.; Watanabe, K.; Taniguchi, T.; Moon, P.; Koshino, M.; Jarillo-Herrero, P.; et al. Massive Dirac fermions and Hofstadter butterfly in a van der Waals heterostructure. *Science* **2013**, *340*, 1427−1430.

(42) Yang, F.; Zibrov, A. A.; Bai, R.; Taniguchi, T.; Watanabe, K.; Zaletel, M. P.; Young, A. F. Experimental determination of the energy per particle in partially filled Landau levels. *Phys. Rev. Lett.* **2021**, *126*, 156802.

(43) Zhang, Y.; Jiang, Z.; Small, J.; Purewal, M.; Tan, Y.-W.; Fazlollahi, M.; Chudow, J.; Jaszczak, J.; Stormer, H.; Kim, P. Landau-level splitting in graphene in high magnetic fields. *Physical review letters* **2006**, *96*, 136806.

(44) Young, A. F.; Dean, C. R.; Wang, L.; Ren, H.; Cadden-Zimansky, P.; Watanabe, K.; Taniguchi, T.; Hone, J.; Shepard, K. L.; Kim, P. Spin and valley quantum Hall ferromagnetism in graphene. *Nat. Phys.* **2012**, *8*, 550−556.

(45) Amet, F.; Williams, J.; Watanabe, K.; Taniguchi, T.; Goldhaber-Gordon, D. Insulating behavior at the neutrality point in single-layer graphene. *Physical review letters* **2013**, *110*, 216601.

(46) Pogna, E. A. A.; Jia, X.; Principi, A.; Block, A.; Banszerus, L.; Zhang, J.; Liu, X.; Sohier, T.; Forti, S.; Soundarapandian, K.; et al. Hot-Carrier Cooling in High-Quality Graphene Is Intrinsically Limited by Optical Phonons. *ACS Nano* **2021**, *15*, 11285−11295.

(47) Walsh, E. D.; Jung, W.; Lee, G.-H.; Efetov, D. K.; Wu, B.-I.; Huang, K.-F.; Ohki, T. A.; Taniguchi, T.; Watanabe, K.; Kim, P.; et al. Josephson junction infrared single-photon detector. *Science* **2021**, *372*, 409−412.

(48) Tielrooij, K.-J.; Piatkowski, L.; Massicotte, M.; Woessner, A.; Ma, Q.; Lee, Y.; Myhro, K. S.; Lau, C. N.; Jarillo-Herrero, P.; van Hulst, N. F.; et al. Generation of photovoltage in graphene on a femtosecond timescale through efficient carrier heating. *Nature Nanotechnol.* **2015**, *10*, 437−443.

(49) Koppens, F.; Mueller, T.; Avouris, P.; Ferrari, A.; Vitiello, M.; Polini, M. Photodetectors based on graphene, other two-dimensional materials and hybrid systems. *Nature Nanotechnol.* **2014**, *9*, 780−793.

(50) Gabor, N. M.; Song, J. C.; Ma, Q.; Nair, N. L.; Taychatanapat, T.; Watanabe, K.; Taniguchi, T.; Levitov, L. S.; Jarillo-Herrero, P. Hot carrier−assisted intrinsic photoresponse in graphene. *Science* **2011**, *334*, 648−652.

(51) Ma, Q.; Lui, C. H.; Song, J. C.; Lin, Y.; Kong, J. F.; Cao, Y.; Dinh, T. H.; Nair, N. L.; Fang, W.; Watanabe, K.; et al. Giant intrinsic photoresponse in pristine graphene. *Nature Nanotechnol.* **2019**, *14*, 145−150.

(52) Kang, D.-H.; Sun, H.; Luo, M.; Lu, K.; Chen, M.; Kim, Y.; Jung, Y.; Gao, X.; Parluhutan, S. J.; Ge, J.; et al. Pseudo-magnetic field-induced slow carrier dynamics in periodically strained graphene. *Nat. Commun.* **2021**, *12*, 5087.

(53) Han, T.; Yang, J.; Zhang, Q.; Wang, L.; Watanabe, K.; Taniguchi, T.; McEuen, P. L.; Ju, L. Accurate Measurement of the Gap of Graphene/h- BN Moiré Superlattice through Photocurrent Spectroscopy. *Phys. Rev. Lett.* **2021**, *126*, 146402.

(54) Cao, B.; Grass, T.; Solomon, G.; Hafezi, M. Optical flux pump in the quantum Hall regime. *Phys. Rev. B* **2021**, *103*, L241301.

(55) Amet, F.; Ke, C. T.; Borzenets, I. V.; Wang, J.; Watanabe, K.; Taniguchi, T.; Deacon, R. S.; Yamamoto, M.; Bomze, Y.; Tarucha, S.; et al. Supercurrent in the quantum Hall regime. *Science* **2016**, *352*, 966−969.

(56) Abanin, D.; Morozov, S.; Ponomarenko, L.; Gorbachev, R.; Mayorov, A.; Katsnelson, M.; Watanabe, K.; Taniguchi, T.; Novoselov, K.; Levitov, L.; et al. Giant nonlocality near the Dirac point in graphene. *Science* **2011**, *332*, 328−330.

(57) Gorbachev, R.; Song, J.; Yu, G.; Kretinin, A.; Withers, F.; Cao, Y.; Mishchenko, A.; Grigorieva, I.; Novoselov, K. S.; Levitov, L.; et al. Detecting topological currents in graphene superlattices. *Science* **2014**, *346*, 448−451.

(58) Uri, A.; Kim, Y.; Bagani, K.; Lewandowski, C. K.; Grover, S.; Auerbach, N.; Lachman, E. O.; Myasoedov, Y.; Taniguchi, T.; Watanabe, K.; et al. Nanoscale imaging of equilibrium quantum Hall edge currents and of the magnetic monopole response in graphene. *Nat. Phys.* **2020**, *16*, 164−170.

(59) Aharon-Steinberg, A.; Marguerite, A.; Perello, D. J.; Bagani, K.; Holder, T.; Myasoedov, Y.; Levitov, L. S.; Geim, A. K.; Zeldov, E.

Long-range nontopological edge currents in charge-neutral graphene. *Nature* **2021**, *593*, 528−534.

(60) But, D.; Mittendorff, M.; Consejo, C.; Teppe, F.; Mikhailov, N.; Dvoretskii, S.; Faugeras, C.; Winnerl, S.; Helm, M.; Knap, W.; et al. Suppressed Auger scattering and tunable light emission of Landau-quantized massless Kane electrons. *Nat. Photonics* **2019**, *13*, 783−787.

(61) Watanabe, K.; Taniguchi, T.; Kanda, H. Direct-bandgap properties and evidence for ultraviolet lasing of hexagonal boron nitride single crystal. *Nat. Mater.* **2004**, *3*, 404−409.

(62) Ferrari, A. C.; Meyer, J. C.; Scardaci, V.; Casiraghi, C.; Lazzeri, M.; Mauri, F.; Piscanec, S.; Jiang, D.; Novoselov, K. S.; Roth, S.; Geim, A. K. Raman Spectrum of Graphene and Graphene Layers. *Phys. Rev. Lett.* **2006**, *97*, 187401.

(63) Pizzocchero, F.; Gammelgaard, L.; Jessen, B. S.; Caridad, J. M.; Wang, L.; Hone, J.; Bøggild, P.; Booth, T. J. The hot pick-up technique for batch assembly of van der Waals heterostructures. *Nat. Commun.* **2016**, *7*, 11894.

(64) Wang, L.; Meric, I.; Huang, P. Y.; Gao, Q.; Gao, Y.; Tran, H.; Taniguchi, T.; Watanabe, K.; Campos, L. M.; Muller, D. A.; Guo, J.; Kim, P.; Hone, J.; Shepard, K. L.; Dean, C. R. One-Dimensional Electrical Contact to a Two-Dimensional Material. *Science* **2013**, *342*, 614−617.

(65) Orlita, M.; Faugeras, C.; Grill, R.; Wysmolek, A.; Strupinski, W.; Berger, C.; de Heer, W. A.; Martinez, G.; Potemski, M. Carrier scattering from dynamical magnetoconductivity in quasineutral epitaxial graphene. *Physical review letters* **2011**, *107*, 216603.

Supporting Information for

Chiral transport of hot carriers in graphene in the quantum Hall regime

Bin Cao,[†,@] Tobias Grass,[‡,@] Olivier Gazzano,[†] Kishan Ashokbhai Patel,[¶] Jiuning Hu,[§] Markus Müller,[†] Tobias Huber-Loyola,[†] Luca Anzi,[¶] Kenji Watanabe,[‖] Takashi Taniguchi,[‖] David B Newell,[§] Michael Gullans,[⊥] Roman Sordan,[¶] Mohammad Hafezi,[*,†,#] and Glenn S Solomon[*,†]

†*Joint Quantum Institute, NIST/University of Maryland, College Park, Maryland 20742, USA*

‡*ICFO-Institut de Ciencies Fotoniques, The Barcelona Institute of Science and Technology, Castelldefels (Barcelona) 08860, Spain*

¶*L-NESS, Department of Physics, Politecnico di Milano, Via Anzani 42, 22100 Como, Italy*

§*National Institute of Standards and Technology, Gaithersburg, Maryland 20878 USA*

‖*National Institute for Materials Science, 1-1 Namiki, 305-0044 Tsukuba, Japan*

⊥*Joint Center for Quantum Information and Computer Science, NIST/University of Maryland, College Park, Maryland 20742 USA*

#*IREAP, University of Maryland, College Park, Maryland 20742, USA*

@*These two authors contributed equally*

E-mail: hafezi@umd.edu; gsolomon@umd.edu

Scattering rates

In the scattering rates, we include both Coulomb interactions and phonon emission: $S_i^{(\text{in})} = S_i^{(\text{in,Coul})} + S_i^{(\text{in,ph})}$ and $S_i^{(\text{out})} = S_i^{(\text{out,Coul})} + S_i^{(\text{out,ph})}$. Within the second-order Markov-Born approximation, the Coulomb scattering terms are given by:

$$S_i^{(\text{in,Coul})} = \frac{2\pi}{\hbar} \sum_{jkl} V_{ijkl}(4V_{klij} - V_{lkij}) \times$$

$$(1 - \rho_j)\rho_k\rho_l\Gamma(\Delta E_{ijkl}), \tag{1}$$

$$S_i^{(\text{out,Coul})} = \frac{2\pi}{\hbar} \sum_{jkl} V_{ijkl}(4V_{klij} - V_{lkij}) \times$$

$$\rho_j(1 - \rho_k)(1 - \rho_l)\Gamma(\Delta E_{ijkl}). \tag{2}$$

Here, V_{ijkl} are the (averaged) Coulomb interaction matrix elements for a scattering process from LLs k and l into LLs i and j. The function $\Gamma(E)$ introduces a step-function broadening of the LLs, $\Gamma(E) = \frac{1}{\pi\Gamma_0}\theta(\Gamma_0 + E)\theta(\Gamma_0 - E)$. For concreteness, we have chosen $\Gamma_0 = 9$ meV,[1] although similar results have been obtained by varying the width in the range between 5 to 10 meV. The energy difference ΔE_{ijkl} refers to the difference $\epsilon_i + \epsilon_j - \epsilon_k - \epsilon_l$ of unbroadened LLs, with $\epsilon_i = \text{sign}(i)\sqrt{2|i|}\frac{\hbar v_F}{l_B}$, where $v_F = 10^6$ m/s and $l_B = 25$ nm$/\sqrt{B}$. The Coulomb interaction matrix elements in graphene can be expressed in terms of Coulomb matrix elements $\tilde{V}_{ijkl}$ of non-relativistic LLs:

$$V_{ijkl} = c_i c_j c_k c_l (\tilde{V}_{|i|,|j|,|k|,|l|} + \tilde{V}_{|i|-1,|j|,|k|,|l|-1} +$$

$$\tilde{V}_{|i|,|j|-1,|k|-1,|l|} + \tilde{V}_{|i|-1,|j|-1,|k|-1,|l|-1}), \tag{3}$$

where we define $C_i = 1$ if $i = 0$, and $c_i = \text{sign}(i)/\sqrt{2}$ elsewise, and $\tilde{V}_{ijkl} = 0$ if any of the indices becomes negative. For positive indices, we employ the pseudopotential model, and define $\tilde{V}_{ijkl}$ as the dominant pseudopotential between the involved LLs, i.e., the pseudopotential which scatters a pair of particles in LLs k and l and at relative angular momentum

$m = 0$ into LLs i and j and relative angular momentum $m' = i + j - k - l$. An explicit construction of the pseudopotential is appended below.

The phonon emission processes are described by the following scattering terms:

$$S_j^{(\text{in,ph})} = \int dE \sum_{i \neq j} \Gamma(\Delta E_{ij} - \hbar\omega)g_0 f(E)\rho_i, \tag{4}$$

$$S_j^{(\text{out,ph})} = \int dE \sum_{i \neq j} \Gamma(\Delta E_{ji} - \hbar\omega)g_0 f(E)(1 - \rho_i) \tag{5}$$

where we assume $g_0 = 36$ THz for an overall coupling frequency, while the scalar function $f(E)$ takes into account an additional energy-dependence of the coupling. Specifically, we assume acoustic phonons in the energy range from 1 meV to 160 meV, with a $1/E$ dependence, see also ref.[2,3] For concreteness, we assume $f(E) = 4$ meV$/E$. In the energy ranges from 170 meV to 175 meV and from 190 meV to 195 meV, optical phonons give rise to an approximately energy-independent coupling, for which we take $f = 1$.

The equilibrium carrier populations are solved from the Bloch equations. The current for different Fermi level is calculated based on the model discussed in the main text. The Fermi level is converted to the gate voltage through a convolution with the Lorentzian-shaped density of states of LLs, assuming a width of $2\Gamma_0$.

Pseudopotentials

In Fourier space, the Coulomb potential reads,

$$V(Q) = \frac{e^2}{8\pi^2\epsilon_0\epsilon_{\text{d}}l_B}\frac{1}{Q} \equiv V_0/(2\pi Q), \tag{6}$$

and the interaction between two electrons at positions $\mathbf{r}_1$ and $\mathbf{r}_2$ is expressed as

$$V = \int d\mathbf{q} V(|\mathbf{q}|)e^{i\mathbf{q}\cdot(\mathbf{r}_1 - \mathbf{r}_2)}. \tag{7}$$

3

Using this expression, the scattering of a pair of electrons from (non-relativistic) LLs n_1 and n_2 into LLs n_3 and n_4 is determined by $\langle mM, n_1 n_2 | \exp[i\mathbf{q} \cdot (\mathbf{r}_1 - \mathbf{r}_2)] | \tilde{m}\tilde{M}, n_3 n_4 \rangle$. Here, $m, \tilde{m}$ is the relative angular momentum of the pair, and $M, \tilde{M}$ their center-of-mass angular momentum. Following Ref,[4] we replace the position operators $\mathbf{r}_i$ by raising operators $a_i^\dagger$ and $b_i^\dagger$, with $a_i^\dagger$ raising the LL quantum number of particle i by one, and $b_i^\dagger$ raising the angular momentum quantum number of particle i by one. Conveniently, we re-write the b operators in the $b_{r,R}$ basis, $b_r = (b_1 - b_2)/\sqrt{2}$ and $b_R = (b_1 + b_2)\sqrt{2}$. We obtain

$$
\begin{aligned}
e^{i\mathbf{q}\cdot(\mathbf{r}_1 - \mathbf{r}_2)} =& e^{-Q^2/2} e^{i\bar{q}a_1^\dagger/\sqrt{2}} e^{iqa_1/\sqrt{2}} e^{-Q^2/2} \\
&\times e^{-i\bar{q}a_2^\dagger/\sqrt{2}} e^{-iqa_2/\sqrt{2}} e^{iqb_r^\dagger} e^{i\bar{q}b_r},
\end{aligned}
\tag{8}
$$

where $Q = |\mathbf{q}|$ and $q = q_x - iq_y$. Since no operator acts on the M quantum numbers, the potential has the form $\delta_{M,\tilde{M}}$. The whole expression reads

$$
\begin{aligned}
V^{n_1 n_2 n_3 n_4}_{m\tilde{m}M\tilde{M}} =& \delta_{M,\tilde{M}} \int d^2\mathbf{q}\, V(\mathbf{q}) e^{-Q^2} \langle m | e^{iqb_r^\dagger} e^{i\bar{q}b_r} | \tilde{m} \rangle \times \\
& \langle n_1 | e^{i\bar{q}a_1^\dagger/\sqrt{2}} e^{iqa_1/\sqrt{2}} | n_3 \rangle \times \\
& \langle n_2 | e^{-i\bar{q}a_2^\dagger/\sqrt{2}} e^{-iqa_2/\sqrt{2}} | n_4 \rangle.
\end{aligned}
\tag{9}
$$

The terms in brakets are evaluated as

$$
\langle n | e^{i\bar{q}a^\dagger/\sqrt{2}} e^{iqa/\sqrt{2}} | \tilde{n} \rangle = \left(\frac{\tilde{n}!}{n!} \right)^{1/2} \left(\frac{iq}{\sqrt{2}} \right)^{n-\tilde{n}} L_{\tilde{n}}^{n-\tilde{n}} \left(\frac{Q^2}{2} \right),
\tag{10}
$$

and

$$
\langle m | e^{iqb_r^\dagger} e^{i\bar{q}b_r} | \tilde{m} \rangle = \left(\frac{\tilde{m}!}{m!} \right)^{1/2} (iq)^{m-\tilde{m}} L_{\tilde{m}}^{m-\tilde{m}} \left(Q^2 \right),
\tag{11}
$$

with $L_n^\alpha(x)$ denoting the generalized Laguerre polynomials. For the scattering matrix elements used in the equations of motion, $\tilde{V}_{n_1 n_2 n_3 n_4}$, we have used the dominant pseudopotential,

4

$\tilde{V}_{n_1 n_2 n_3 n_4} \equiv V^{n_1 n_2 n_3 n_4}_{m \tilde{m} M \tilde{M}}$ with $m = 0$, $\tilde{m} = n_1 + n_2 - n_3 - n_4$, and arbitrary $M = \tilde{M}$.

Transport and PC measurements

Transport measurements

In Fig. S1, we show optical pictures and mobility fittings with transport measurements of the two samples at 4 K. Two samples are of sizes 3.5×3.5 μm and 9×9 μm respectively and the fitted mobilities of both samples[5] are about 13000 cm^2/Vs.
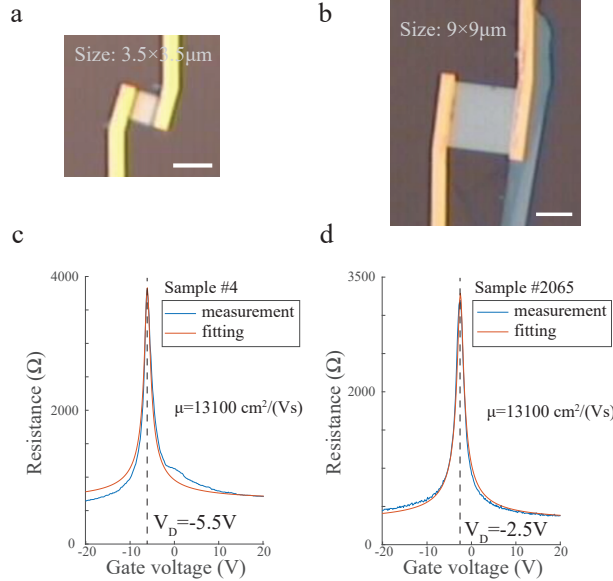
Figure S1: Optical images of the two studied samples and their transport measurements without a magnetic field. **a,b**, Optical images of sample #4 and #2065, respectively. White scale bars: 5 μm. **c,d**, Corresponding transport measurements of the two samples at 4 K with fittings. Their Dirac points are located at $V_D = -5.5, -2.5$ V respectively. Contact resistance for sample #4 is 650 Ω whereas 288 Ω for sample #2065.

The Landau fans for the two samples, obtained from transport measurements within magnetic fields, are shown in Fig. S2. Since the samples are two-terminal, the measured is a combination of Hall and the longitudinal conductance[6–8] and we plot the derivative with respect to gate voltage dG/dV. In Fig. S2b, we fit the even-fillings of the LLs and use them to benchmark the PC Landau fan plotted in Fig. 2a. In addition, we plot the transport

measurement at 9 T in Fig. S2c which shows no symmetry-broken features. Transport measurements with/without optical illumination show no difference.
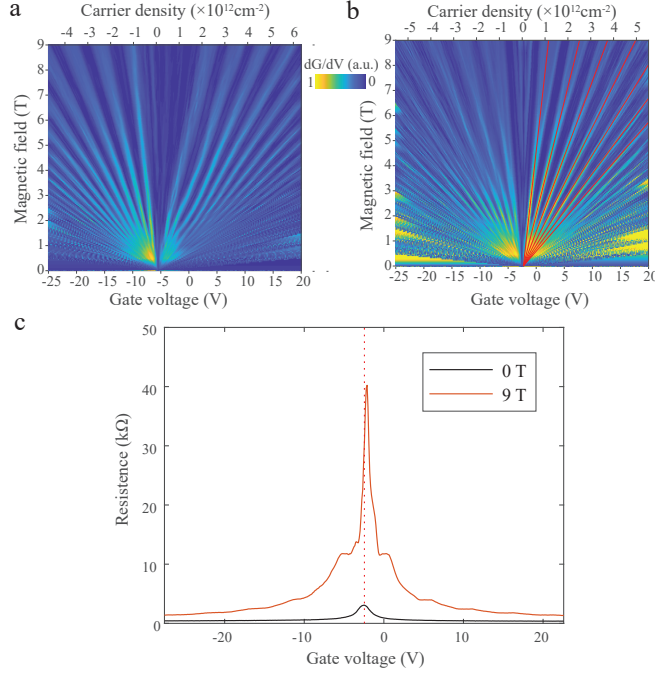

Figure S2: Landau fan obtained from transport measurements for both samples. **a**, Landau fan obtained from transport measurements for sample #4; **b**, Landau fan obtained from transport measurements for sample #2065. dG/dV is plotted since the samples are two-terminal.[9] The red lines are fitted even-fillings which are used in Fig. 2a. **c**, Resistance for sample #2065 measured at 9 T. 0 T result is included for comparison. In the transport measurements, there is no miniband appearing and the feature corresponding to LL_0 does not split, indicating that there is no symmetry-broken states near the Dirac point. The Dirac point is marked by the vertical dashed line.

TIA

In Fig. S3, we show the circuit of the home-made TIA. Calibrations show that the TIA has a linear conversion from current (0 to 100 nA) to voltage with a constant ratio which is independent of the sample impedance.
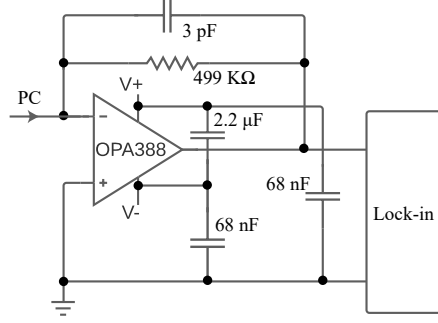
Figure S3: Circuit design of the TIA. Three capacitors of 2.2 µF, 68 nF and 68 nF are used to stabilize the circuit. The PC is measured using the TIA and the output voltage is measured with the voltage channels of a frequency-locked lock-in amplifier.

The function of TIA is to remove the impact of the substantially varying sample resistance[10] from the measurements of PC. In the quantum Hall regime, the resistance of a two-terminal rectangular graphene sample is given by the quantized value $R_K/(4\nu+2)$ within the plateaus regime below $\mathrm{LL}_{\nu+1}$, where $R_K = h/e^2 \approx 26$ kΩ[11,12] and the resistance is even higher near the Dirac point, as shown in Fig. S2c. In comparison, the input impedance of common commercial current preamplifier (e.g. SR570) with a similar sensitivity is between 100 Ω and 10 kΩ, which is comparable to the sample's impedance. Similarly, the input impedance of the current channel of lock-in amplifiers is also high: 1 kΩ for SR530, 100 Ω/1 kΩ for SR860. As a result, when E_F is swept through many LLs, the impedance of the sample changes dramatically and thus an artificial envelope is imposed to the measured PC, making measurements inaccurate if without a TIA. Comparison of PC measurements with and without TIA is plotted in Fig. S4, where the inaccuracy of measuring PC directly with a lock-in amplifier is clearly demonstrated.
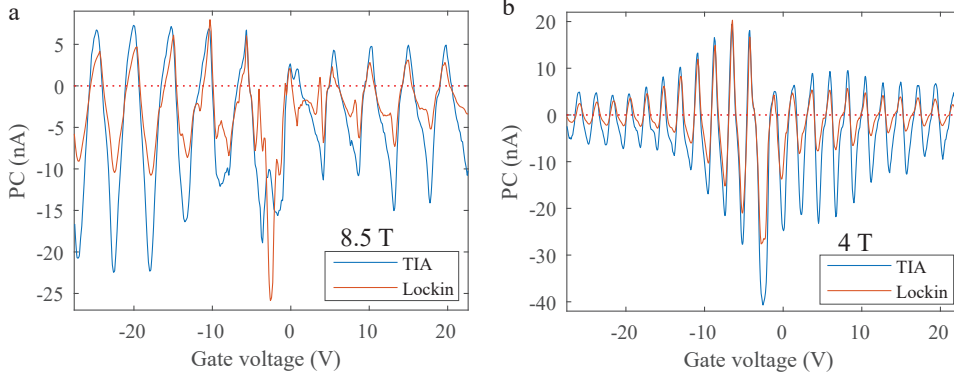
7

Figure S4: Illustration of the importance of the TIA. **a**, Comparison between the PC measured through the TIA versus with the lock-in amplifier's current channel at 8.5 T for sample #2065. **b**, Comparison between the PC measured through the TIA versus with the lock-in amplifier's current channel at 4 T for sample #2065. Significant difference in the envelope is observed. In addition, PC measured without the TIA cannot recover the dip at the Dirac point at 8.5 T. These comparisons demonstrate that a TIA is necessary for precise PC measurements in graphene in the quantum Hall regime.

To show the function of TIA in the PC measurements, we compare PC obtained through a TIA and directly from the current channel of the lock-in amplifier (SR530), which has an impedance of 1 kΩ. At a high magnetic field of 8.5 T, measurement without TIA, as shown in Fig. S4a, shows weaker PC values on the majority carrier side and the PC peaks are not asymmetric. This does not reflect the mechanism of carriers' relaxation as discussed in the main text. On the other hand, measurements using a TIA shows less noise. This is expected as a TIA does no exhibit the usual Johnson–Nyquist noise.[13] In addition, the PC dip at the Dirac point revealed by TIA measurements does not appear because of the divergence of sample's longitudinal impedance at the Dirac point,[8,14] obscuring another important feature. The data at low field strength is shown in Fig. S4b. Measurements without a TIA shows a faster decaying envelope of PC oscillations, as E_F is moved away from the Dirac point, compared to the accurate one measured using a TIA.

8

PC measurements

In order to differentiate the part of the PC which depends on the orientation of B from the orientation-independent one, we subtract and sum the PC measured at $+B$ and $-B$: [PC($+B$)-PC(-B)]/2; [PC($+B$)-PC(-B)]/2. The substation has been shown in Fig. 1b. The sum is shown in Fig. S5 representing the orientation-independent part of PC. As one can see, the orientation-independent part of PC is minimal compared to the dependent part, confirming that the transport of carriers are prominently through chiral edge states. The orientation-independent part of PC is attributed to the direct diffusion of carriers to the contacts.[15]
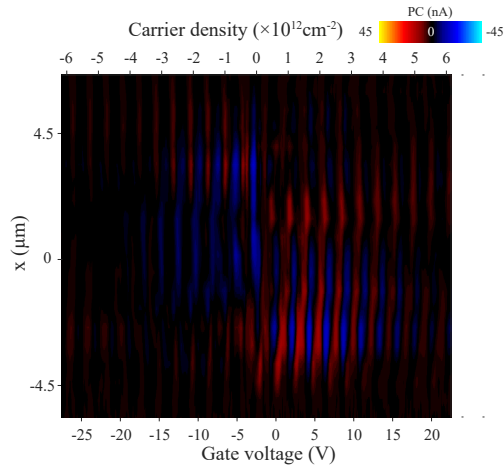

Figure S5: Part of PC which is independent from the orientation of the B-field . The sum of the PCs measured at +4.5 T and -4.5 T, as a function of x and gate voltage. The amplitude of the sum is minimal, compared to the subtraction shown in Fig. 1b.

The PC as a function of gate voltage and field strength (PC Landau fan) for sample #2065, measured at a laser power of 1 µW, has been shown in Fig. 2. We measure the PC Landau fan with a laser power up to 8 µW and the same oscillation behavior, as reported in the main text, is reliably observed. For example, PC Landau fan for laser powers of 0.3 µW and 2 µW are shown in Fig. S6. In addition, we see minimal PC when $B = 0$, distinguishing our observations from PC generated by inhomogeneity or PN junctions.[16]
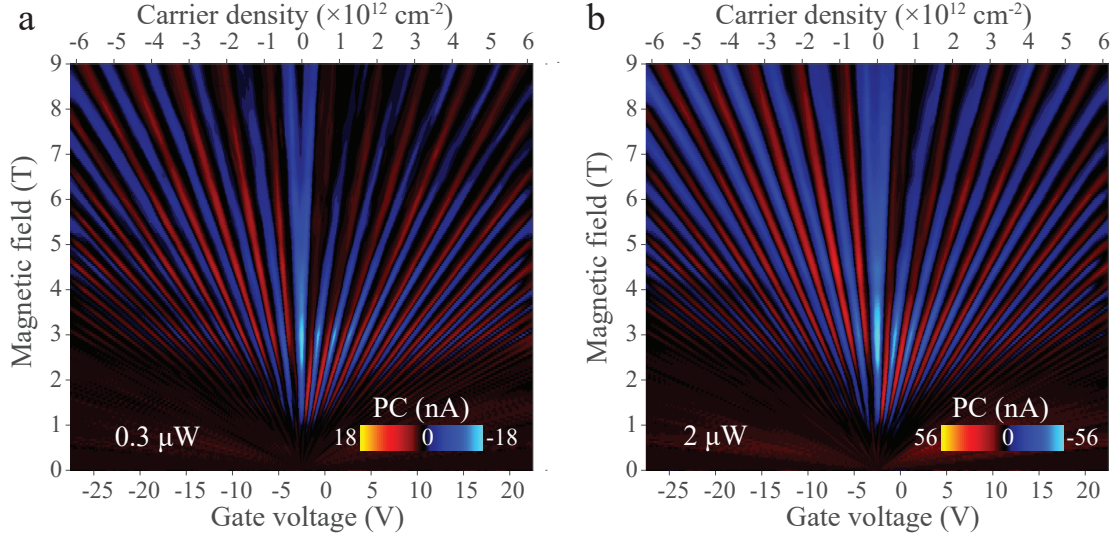
Figure S6: PC Landau fan for sample #2065. **a**, PC Landau fan measured at 0.3 μW. **b**, PC Landau fan measured at 2 μW. They show the same oscillation behavior as reported in the main text.

We also show the PC Landau fan for sample #4 in Fig. S7. Features discussed in the main text are repeated, except the dip of the PC at the Dirac point. This is because Fig. S7 is obtained directly with the lock-in amplifier's current channel without a TIA and calibrated afterwards to reflect the accurate envelope. However the dip at the Dirac point cannot be recovered by a simple calibration.
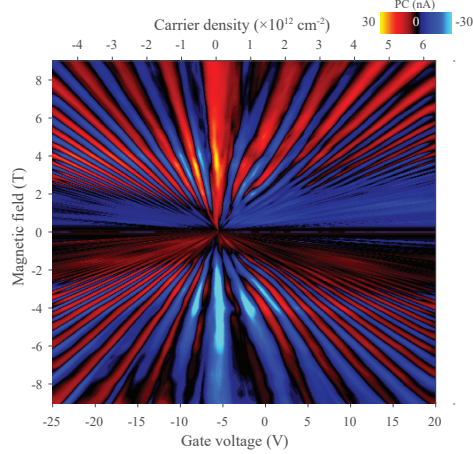
Figure S7: PC Landau fan for sample #4. Features agree with the presented analysis in the main text, except the missing dip at the Dirac point at high field strength. This is expected because this particular PC Landau fan was firstly measured directly using the lock-in and then corrected using the parameters of the TIA and thus the dip in the 0th LL at high field strength does not appear as a result of the obscuration with the sample impedance.

We also see a peculiar double-bent saturation behavior which occurs predominately at high LLs, as shown in the inset of Fig. S8. Similar behavior has been observed in a high power pulsed regime[17] which is attributed to the efficient Coulomb scattering processes at the pumped energies. However, we observe at much lower intensities here possibly due to the continuous pump we are using, which constantly excites carriers and thus enhances the Coulomb interactions. We note that the double-bent saturation is sensitive with position and the exact mechanism needs further study of the impacts from sample sizes and disorder strength, etc.
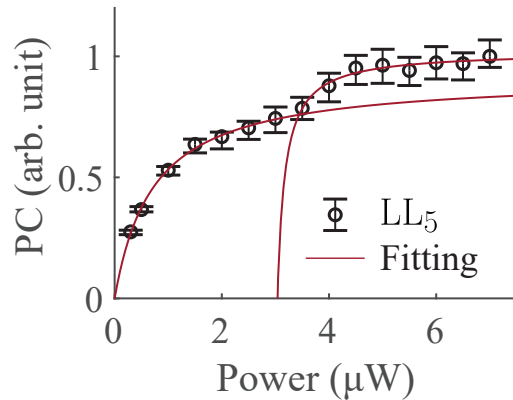
Figure S8: Double saturation of PC for high LLs at certain positions. For some high LLs at certain positions, a peculiar double saturation is observed.

Laser power and polarization stabilization

The laser power is constantly monitored with a photodiode right before the beam enters the optical window and a feedback is given to a PID loop controlling a laser power control module. The power control module is home-made using a liquid-crystal retarder and a polarizer. The frequency of the power stabilization is tuned such that the power is still chopped mechanically at 308 Hz while remains stable over each measurement duration, which is usually longer than 1 s. In total, power fluctuation can be controlled within 0.5%. The polarization stabilization is achieved by diffracting the beam on a grating imprinted on a liquid-crystal spatial light modulator, which only works with a linear polarized light, and we only use the first order of diffraction. This ensures the polarization of the beam is clean and this is done before the photodiode used for the power stabilization.

Wavelength dependence of PC measurements

By changing excitation wavelength from 940 nm to 870 nm, we see little change in the PC measurements. In Fig. S9, we show measurements at 940 nm with a power of 2 μW and at 870 nm with powers of 1.71 and 2 μW. Measurements with different wavelengths match well, whereas PC peaks at different LLs show different scalings with power as explained in

the main text.

The reason for selecting 1.71 μW to compare with 2 μW is the following. Since the wavelength is changed, the laser focal spot size is changed accordingly. To maintain the average intensity same as 940 nm with 2 μW, one power for 870 nm is chosen as $(870/940)^2 \times 2$ μW $= 1.71$ μW.
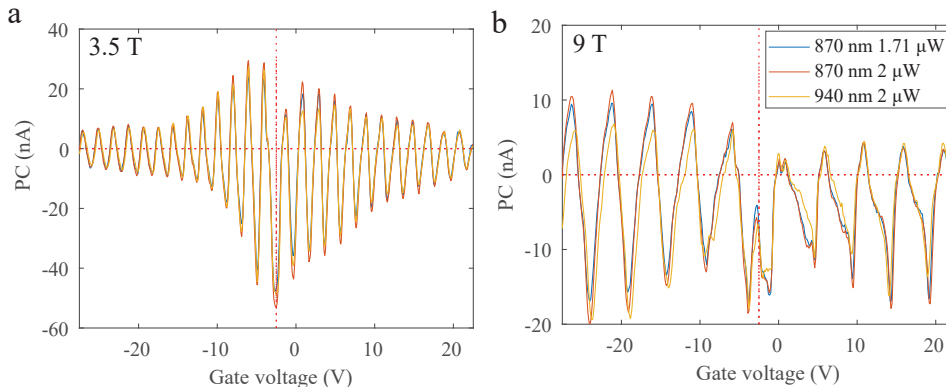

Figure S9: Wavelength dependence of PC measurements. **a**, PC measurements with excitation wavelength of 870 nm with laser powers 1.71, 2 μW and 940 nm with 2 μW, at 3.5 T are shown. **b**, Same results for 9 T. PCs measured at excitation wavelength of 870 nm and 940 nm overlap well, indicating that LLs, resonant to the excitation wavelength, merge together.

References

(1) Wendler, F.; Knorr, A.; Malic, E. Carrier multiplication in graphene under Landau quantization. *Nature communications* **2014**, *5*, 3703.

(2) Wendler, F.; Knorr, A.; Malic, E. Ultrafast carrier dynamics in Landau-quantized graphene. *Nanophotonics* **2015**, *4*, 224–249.

(3) Malic, E.; Knorr, A. *Graphene and carbon nanotubes: ultrafast optics and relaxation dynamics*; John Wiley & Sons, 2013.

(4) Macdonald, A. H. Introduction to the physics of the quantum Hall regime. *arXiv preprint cond-mat/9410047* **1994**,

(5) Kim, S.; Nah, J.; Jo, I.; Shahrjerdi, D.; Colombo, L.; Yao, Z.; Tutuc, E.; Banerjee, S. K. Realization of a high mobility dual-gated graphene field-effect transistor with Al 2 O 3 dielectric. *Applied Physics Letters* **2009**, *94*, 062107.

(6) Abanin, D. A.; Levitov, L. S. Conformal invariance and shape-dependent conductance of graphene samples. *Physical Review B* **2008**, *78*, 035416.

(7) Williams, J. R.; Abanin, D. A.; DiCarlo, L.; Levitov, L. S.; Marcus, C. M. Quantum Hall conductance of two-terminal graphene devices. *Physical Review B* **2009**, *80*, 045408.

(8) Sarma, S. D.; Adam, S.; Hwang, E.; Rossi, E. Electronic transport in two-dimensional graphene. *Reviews of modern physics* **2011**, *83*, 407.

(9) Bolotin, K. I.; Ghahari, F.; Shulman, M. D.; Stormer, H. L.; Kim, P. Observation of the fractional quantum Hall effect in graphene. *Nature* **2009**, *462*, 196–199.

(10) Horowitz, P.; Hill, W. *The art of electronics*; Cambridge university press Cambridge, 2002.

(11) Zhang, Y.; Tan, Y.-W.; Stormer, H. L.; Kim, P. Experimental observation of the quantum Hall effect and Berry's phase in graphene. *nature* **2005**, *438*, 201–204.

(12) Goerbig, M. Electronic properties of graphene in a strong magnetic field. *Reviews of Modern Physics* **2011**, *83*, 1193.

(13) Donati, S. *Photodetectors: devices, circuits and applications*; John Wiley & Sons, Hoboken, 2021.

(14) Abanin, D. A.; Novoselov, K. S.; Zeitler, U.; Lee, P. A.; Geim, A. K.; Levitov, L. S. Dissipative quantum Hall effect in graphene near the Dirac point. *Physical review letters* **2007**, *98*, 196806.

(15) Song, J. C.; Levitov, L. S. Shockley-Ramo theorem and long-range photocurrent response in gapless materials. *Physical Review B* **2014**, *90*, 075415.

(16) Gabor, N. M.; Song, J. C.; Ma, Q.; Nair, N. L.; Taychatanapat, T.; Watanabe, K.; Taniguchi, T.; Levitov, L. S.; Jarillo-Herrero, P. Hot carrier–assisted intrinsic photoresponse in graphene. *Science* **2011**, *334*, 648–652.

(17) Winzer, T.; Mittendorff, M.; Winnerl, S.; Mittenzwey, H.; Jago, R.; Helm, M.; Malic, E.; Knorr, A. Unconventional double-bended saturation of carrier occupation in optically excited graphene due to many-particle interactions. *Nature communications* **2017**, *8*, 1–6.